Computational Kinetics Simulation of the Dissolution and Coarsening in the HAZ during Laser Welding of 6061-T6 Al-Alloy

Experimental results indicate it is possible to predict HAZ hardness of heat-treatable aluminum alloys

BY A. D. ZERVAKI AND G. N. HAIDEMENOPOULOS

ABSTRACT. Laser beam welding (LBW) has become common practice in the production lines of several industrial sectors including the electronics, domestic appliances, and automotive industries. The advantages of LBW over conventional fusion welding processes (mainly GMAW and GTAW) is the lower welding heat input and smaller weld pool and HAZ dimensions, which are associated with lower residual stresses and distortion. In addition to the general problems encountered during the application of LBW on aluminum alloys (high reflectivity, porosity, loss of alloying elements), the most important problem, which concerns the heat treatable alloys, is the softening of the HAZ due to the dissolution and coarsening of the strengthening precipitates. The main objective of the present work is the simulation of the microstructural evolution in the HAZ in order to predict the hardness drop of the HAZ as a function of welding conditions. Models for the numerical simulation of precipitation, dissolution, and coarsening of β-Mg_2Si phase were developed and solved with the use of the computational thermodynamics and kinetics software *DICTRA*. In this way the volume fraction and average precipitate size were calculated for several types of weld thermal cycles, under extremely nonisothermal conditions. Calculated hardness profiles in the HAZ are in good agreement with the experimental values. The above results point to the conclusion that it is possible to simulate the microstructure evolution and hardness in the HAZ of aluminum laser welds, thus opening the way for a more precise control and design of LBW of aluminum alloys.

Introduction

Fusion welding of heat-treatable aluminum alloys, which are strengthened through precipitation hardening, is accompanied by a loss of strength in the HAZ. This degradation often limits the application of welding in these alloys. Laser beam welding (LBW) has been recently applied successfully (Refs. 1, 2) for the welding of airframe components. A series of experiments on LBW of 6xxx alloys has been carried out (Ref. 3) in order to support current work regarding the effect of welding parameters on weld penetration, as well as the size and hardness of HAZ. Complete joint penetration welds in 6061-T6 were obtained with HAZ width of 2 mm. However, despite the limited HAZ dimensions, a drop in HAZ hardness is still apparent. Softening in the HAZ is normally attributed to dissolution and/or coarsening of the strengthening precipitates. Heat-affected zone softening is a common and more pronounced effect when welding with conventional welding

A. D. ZERVAKI and G. N. HAIDEMENOPOULOS are with Department of Mechanical and Industrial Engineering, University of Thessaly, Pedion Areos, Volos, Greece.
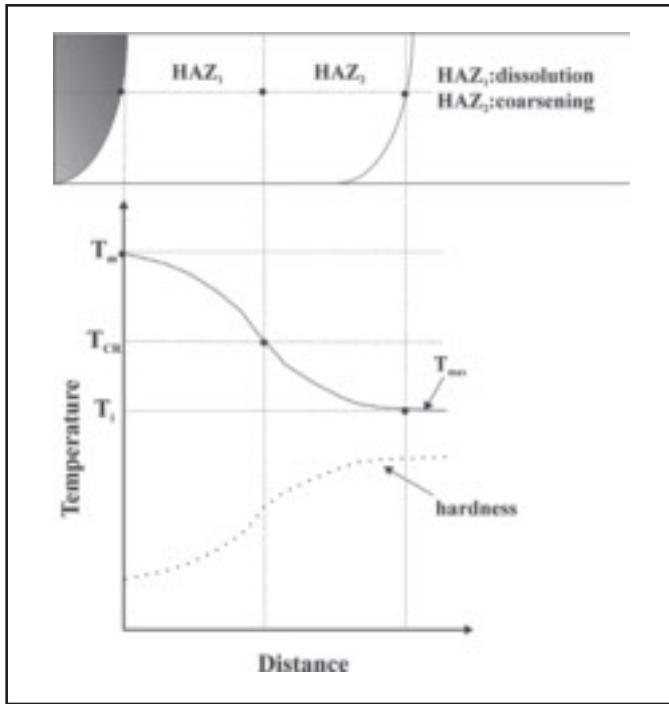
Fig. 1 — Maximum temperature and corresponding hardness profile in the HAZ due to dissolution and coarsening (T_{CR} = 400°C, T_i=room temperature, T_m = solidus temperature).
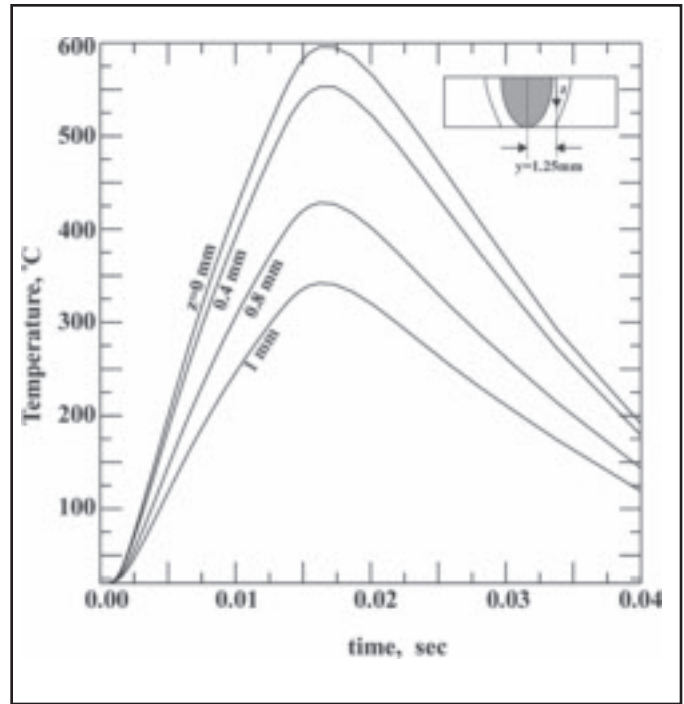

Fig. 2 — Thermal cycles in the HAZ (z = 0 lies on the upper surface of the sheet). Experimental conditions: laser power = 4500 W, weld speed = 4.8 m/min, h = 56 J/mm.

processes. Kou (Ref. 4) observed a hardness minimum in the HAZ of 6061 alloy welded in the artificially aged (T6) or naturally aged (T4) conditions by GTAW and attributed the softening to coarsening of β″precipitate, the basic strengthening precipitate, and formation of the coarser β′ precipitate. Similar results have been reported by Malin (Ref. 5) on gas-metal-arc-welded (GMAW) 6061-T6 aluminum alloy. The aim of the present paper is to simulate the softening reactions (dissolution and coarsening) in the HAZ of laser-beam-welded 6061-T6 by a finite-element-based heat flow analysis of weld thermal cycles combined with a computational diffusional kinetics analysis of dissolution and coarsening. The latter was performed by applying the *DICTRA* methodology (Ref. 6), a software tool for handling diffusion in multicomponent, multiphase systems based on the numerical solution of the diffusion equations with local thermo-

dynamic equilibrium at the phase interfaces. Several models have been developed in recent years to describe diffusional phase transformations in aluminum alloys. The majority of the models deal with isothermal transformations (Refs.7, 8). Relatively few research efforts have been directed toward modeling of non-isothermal transformations as those encountered in welding (Refs. 9–14). The *DICTRA* methodology mentioned above has been applied by Agren (Ref. 15) for the modeling of carbide dissolution in steels under isothermal conditions. Also, *DICTRA* has been applied for the solution of coarsening problems under isothermal conditions (Refs. 16–19). A new coarsening model presented in Ref. 17 was implemented in *DICTRA*. The model was based on the assumption that coarsening of a system can be described by performing calculations on a particle of maximum size at the center of a spherical cell. The

maximum particle size is 1.5 times the average size according to the LSW theory of coarsening by Lifshitz and Slyozov (Ref. 20) and Wagner (Ref. 21). In Ref. 17, the model was applied for the description of the coarsening behavior of carbo-nitrides in multicomponent Cr-steels under isothermal conditions.

In the present paper, *DICTRA* was used for the simulation of dissolution, re-precipitation, and coarsening during the welding thermal cycle in the HAZ of 6061-T6 laser welds. The thermal cycles in the HAZ were calculated by the finite element method. The results of the heat flow analysis are compared with experimental data regarding the weld pool shape. The calculated thermal cycles were linearized and used as input for the *DICTRA* simulations. The major assumptions made are the following:

1) The HAZ is divided into two parts (Fig. 1): HAZ$_1$ where the maximum tem-
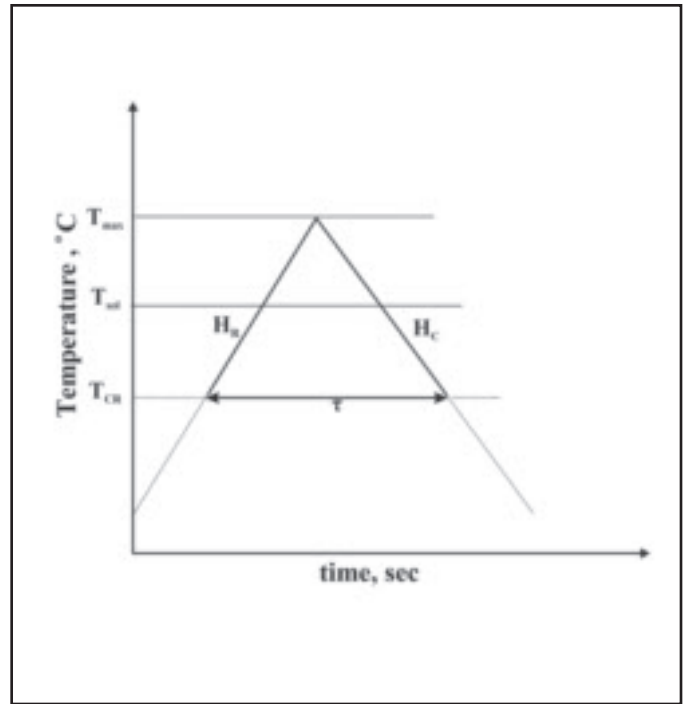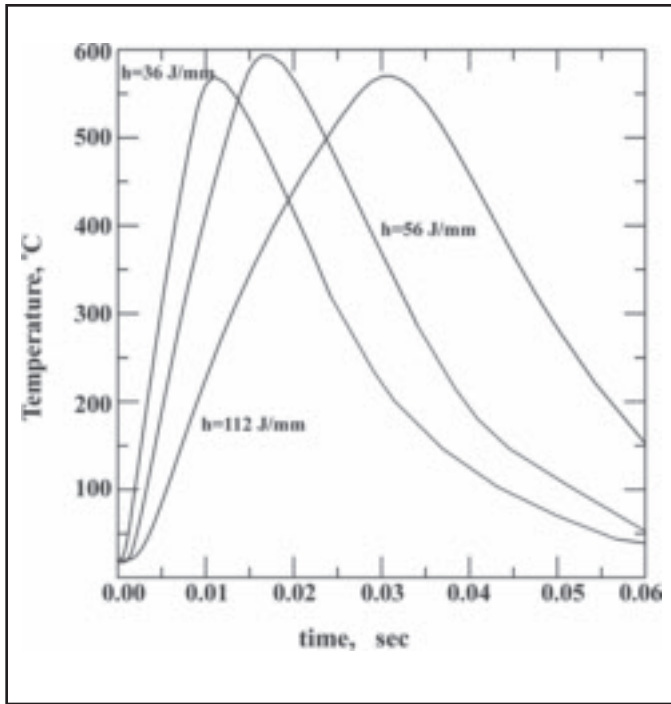
Fig. 3 — Thermal cycles at the boundary HAZ/weld pool interface for three values of heat input at the surface of the plate.

Fig. 4 — Schematic representation of weld thermal cycle as used in dissolution simulations.

Table 1 — Values of the Thermal Cycle Parameters Used for the Dissolution Simulations

T_{max} (°C)	H_C/H_R (°C/s)	τ (s)
595	10^3–5×10^7	7.8×10^{-6}–0.39
575	10^3–5×10^7	7×10^{-6}–0.35
550	10^3–5×10^7	6×10^{-6}–0.3
500	500–10^6	2×10^{-4}–0.4
450	500–10^6	10^{-4}–0.2

perature of the welding cycle exceeds T_{CR} and where only dissolution during heating and reprecipitation during cooling can occur. In HAZ_2, on the other hand, the maximum temperature does not exceed T_{CR} and only precipitate coarsening can occur. $T_{CR} = 400°C$ is an arbitrary critical temperature, above which it is assumed that precipitation dissolution dominates, and below which precipitate coarsening dominates.

2) Although the primary strengthening phases are the metastable phases β″ and β′, only the equilibrium precipitate β-Mg₂Si was considered in the simulations, since kinetic data for the metastable phases (GP-zones, β″, β′) are not yet included in the relevant databases.

Welding Thermal Cycles

The temperature distribution and the associated thermal cycles were calculated by employing the general-purpose finite element program *ABAQUS* (Ref. 22). A three-dimensional geometry was employed. The boundary conditions involved heat losses due to convection and radiation. The latent heat of fusion was taken into account. The laser heat source was modeled as a moving Gaussian energy distribution attenuated in the plate thickness direction to account for the keyhole effect. The details of the heat flow analysis are presented elsewhere (Ref. 3). The evaluation of the model was accomplished by comparing the predicted weld pool shape with the experimentally determined shape by metallography. Calculated weld ther-

mal cycles are shown in Fig. 2 for various z-positions in the HAZ of 6061-T6. The effect of heat input on the resulting thermal cycle is shown in Fig. 3, which depicts the thermal cycles at the HAZ/weld pool interface at the surface of the plate. It is evident that a lower heat input results in a steeper thermal cycle. The major parameters characterizing the thermal cycle at each point in the HAZ are the maximum temperature, the cycle duration, as well as the heating and cooling rates, respectively. These parameters were evaluated and were used as an input in the simulation of dissolution and coarsening discussed in the next sections.

Simulation of Disolution during Laser Welding of 6061-T6

The weld thermal cycle used in the dissolution simulations was linearized as depicted in Fig. 4. In the Figure, T_{max} is the maximum temperature of the cycle, T_{sol} is
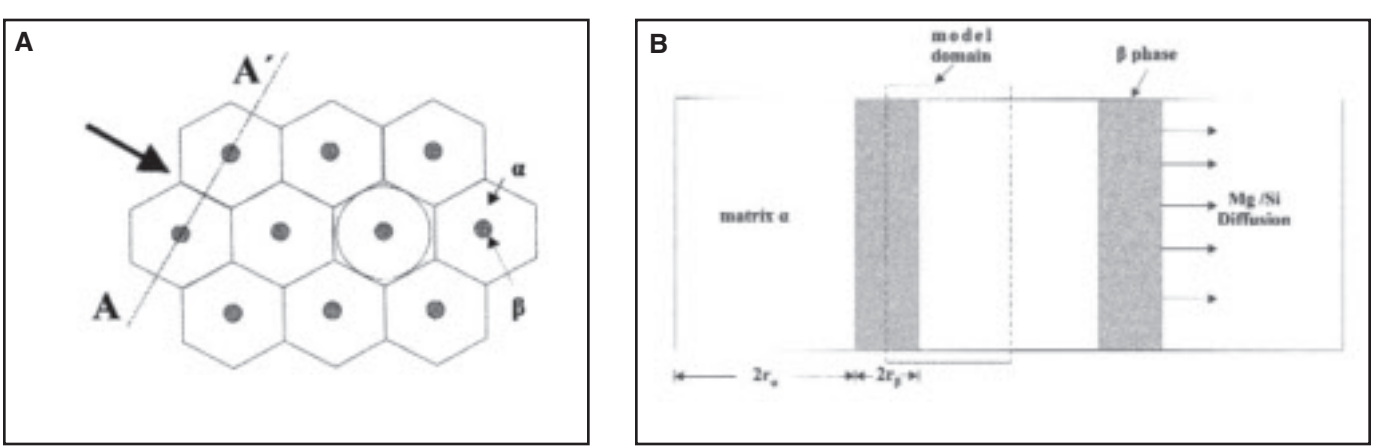
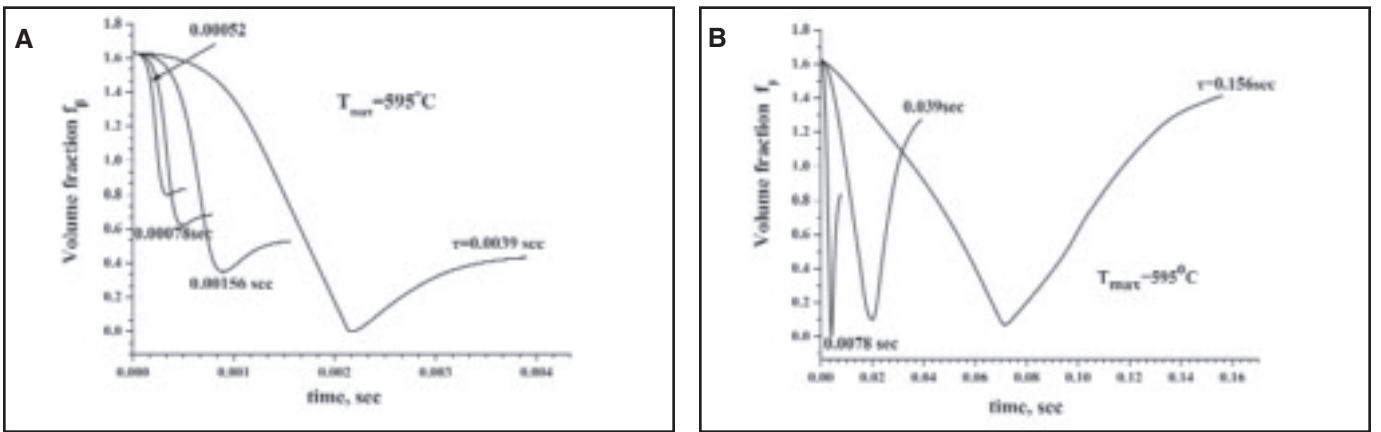*Fig. 5 — Geometrical model of dissolution simulations. A — Plan view; B — cross section.*

Fig. 6 — Volume fraction (f_β) variation vs. time for r_β^0 =2nm. A — Short cycles; B — longer cycles.

the solvus temperature, T_{CR} = 400°C, τ is the cycle duration, while H_R and H_C are the heating and cooling rates, in °C/s, respectively. The duration of the thermal cycle is given by the relation

$$\tau = \left(T_{max} - T_{CR}\right)\left(\frac{1}{H_C} + \frac{1}{H_R}\right) \quad (1)$$

The parameters of the thermal cycle used in the simulations are given in Table 1. The dissolution problem is treated here using the *DICTRA* methodology. The relevant geometrical model is shown in Fig. 5. The rod morphology of the β-Mg$_2$Si precipitate requires the use of cylindrical geometry. In the geometrical model, r_α and r_β are the radius of the α and β phase regions, respectively. The geometry of Fig. 5B follows the cell model proposed by Grong (Ref. 11), shown in Fig. 5A , where each β-

particle is surrounded by its own hexagonal cell and the dissolution region for the α-phase is represented by an inscribed cylinder with volume equal to that of the hexagonal cell. Due to symmetry reasons only the prescribed calculation area in Fig. 5B is considered. Surface energy effects were not taken into account since it was considered that dissolution of precipitates is driven mainly by differences in chemical free energy. For a given volume fraction of β-phase, the sizes of the α (r_α) and β (r_β) regions are related by the expression

$$r_\alpha = \left(\frac{1}{f_\beta^{1/2}} - 1\right)r_\beta \quad (2)$$

where f_β is the volume fraction of the β-phase.

Further assumptions are the following:

• The problem was considered to be one-dimensional where dissolution takes place only in the radial direction.

• Because Mg diffuses much slower than Si in the α-phase, it was considered that only Mg diffusion controls the dissolution rate.

• The β-precipitate was considered stoichiometric, and therefore, no diffusion was considered within the β-phase.

• Depending on the amount of the β-phase dissolved during the heating part of the thermal cycle, reprecipitation of that phase occurs during the cooling part of the thermal cycle.

The initial compositions of the α and β phases are calculated by the *Thermo-Calc* software (Ref. 23) and obey the mass balance equations

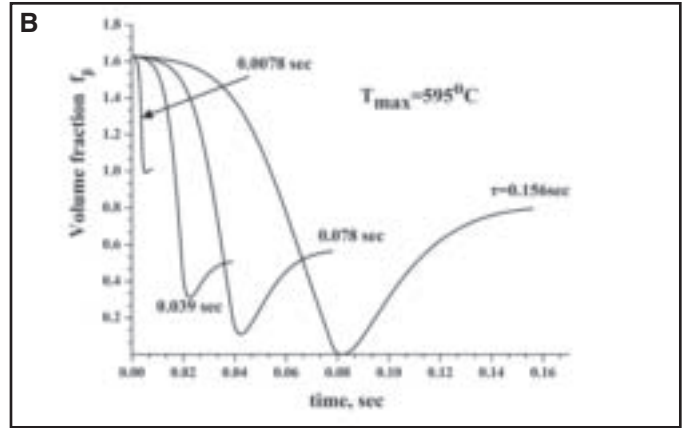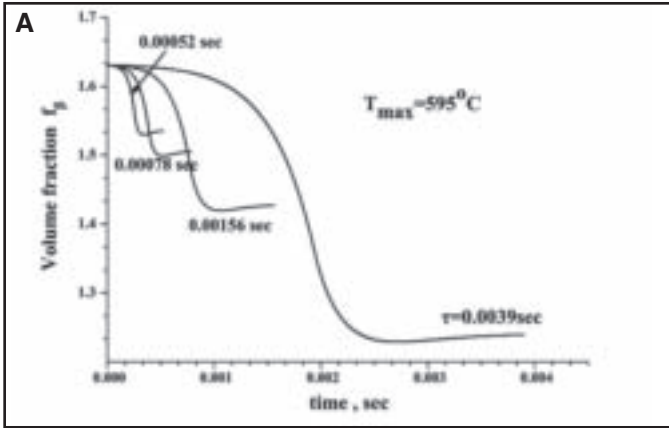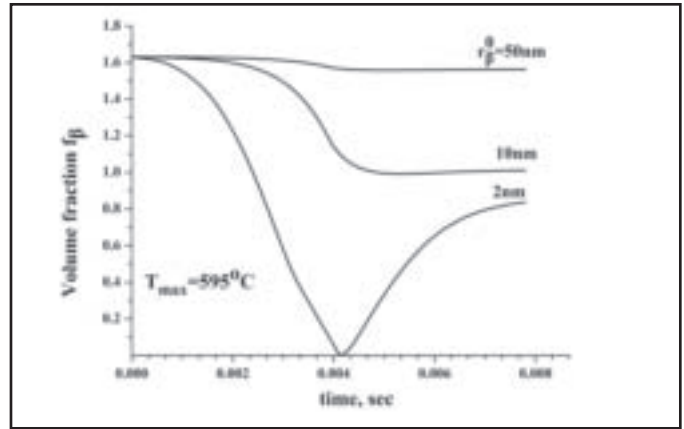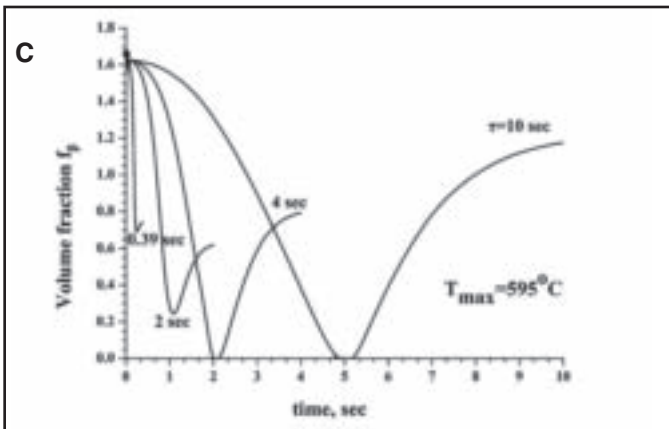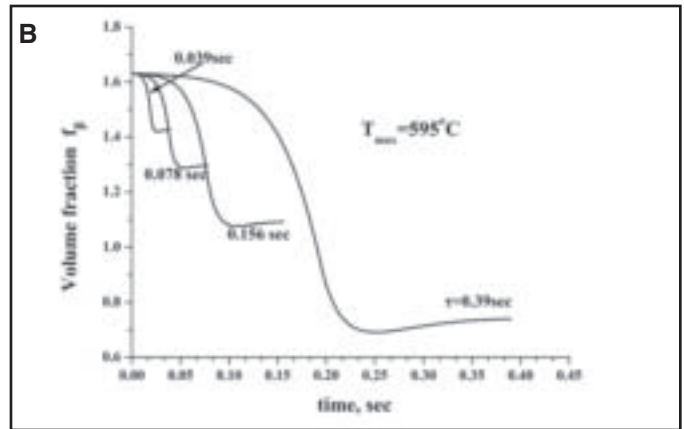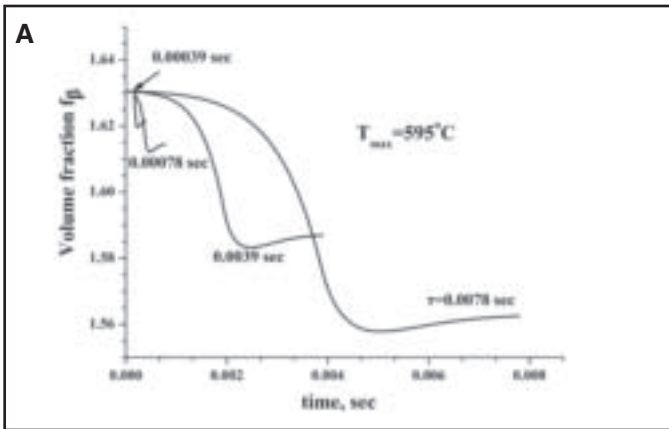Fig. 7 — Volume fraction (f_β) variation vs. time for r_β^o =10 nm . A — Short cycles; B — longer cycles.

Fig. 8 — Volume fraction (f_β) variation vs. time for r_β^0=50nm. A — Short cycles; B — medium cycles; C — long cycles.

Fig. 9 — Volume fraction (f_β) variation vs. time for r_β^0 =2, 10, 50 nm (cycle duration = 7.8 ms).

$$r_\alpha^0 C_{Mg}^{\alpha,0} + r_\beta^0 C_{Mg}^{\beta,0} = C_{Mg}^0 \qquad (3)$$

$$r_\alpha^0 C_{Si}^{\alpha,0} + r_\beta^0 C_{Si}^{\beta,0} = C_{Si}^0 \qquad (4)$$

where r^0_α and r^0_β are the initial sizes of the α and β phases, respectively. $C_{Mg}^{\alpha,0}$ and $C_{Mg}^{\beta,0}$ are the initial Mg contents of the α and β phases, respectively. $C_{Si}^{\alpha,0}$ and $C_{Si}^{\beta,0}$ are the initial Si contents of the α and β phases, respectively. C_{Mg}^0 and C_{Si}^0 are the Mg and Si alloy contents, respectively.

The Mg diffusion in the α-phase ($0<r<r_\alpha$) is described by the following equation:

$$\frac{\partial C_{Mg}^\alpha}{\partial t} = \frac{1}{r}\frac{\partial}{\partial r}\left(r D_{Mg}^\alpha \frac{\partial C_{Mg}^\alpha}{\partial r} \right) \qquad (5)$$

where C_{Mg}^α and D_{Mg}^α are the Mg content and the diffusion coefficient of Mg in α-phase, respectively. The flux balance at the
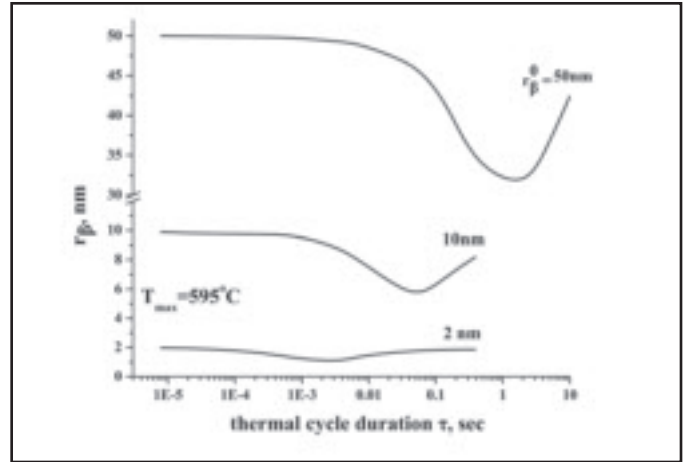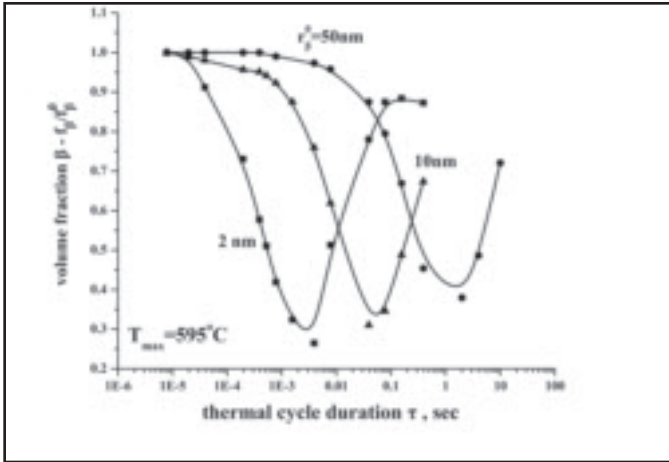
Fig. 10 — Variation of volume fraction of β vs. thermal cycle duration (τ) and initial size at T_{max}= 595°C.

Fig. 11 — Variation of mean radius of β vs. thermal cycle duration (τ) and initial size (T_{max} = 595°C).
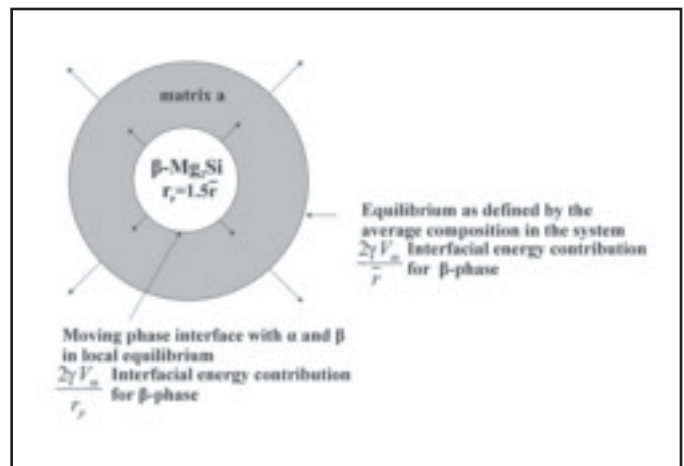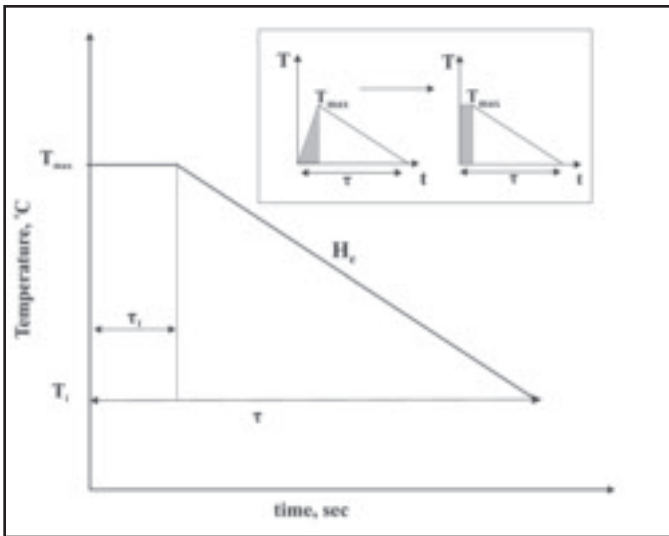

Fig. 12 — Schematic representation of the weld thermal cycle, incorporated in the coarsening calculations.

Fig. 13 — Schematic picture of the coarsening model incorporated in DICTRA.

α/β interface is described by the equation

$$u_{\alpha/\beta}\left(C_{\beta}^{\alpha/\beta} - C_{\beta}^{\alpha/\beta}\right) = D_{Mg}^{\alpha}\left(\frac{\partial C_{Mg}^{\alpha}}{\partial r}\right)_{\alpha/\beta} \quad (6)$$

where $u_{\alpha/\beta}$ is the velocity of the α/β interface and $C_{\beta}^{\alpha/\beta}$, $C_{\alpha}^{\alpha/\beta}$ are the Mg concentrations of the α and β phases at the α/β interface.

For this closed system, the boundary conditions are

$$\frac{\partial C_{Mg}}{\partial r}\bigg|_{r=0} = 0 \quad \text{and} \quad (7)$$

$$\frac{\partial C_{Mg}}{\partial r}\bigg|_{r=r_a+r_\beta} = 0 \quad (8)$$

The initial condition is given by

$$C_{Mg}^{\alpha}(r,0) = 0.98 \quad \text{for } 0 \le r \le r_\alpha \quad (9)$$

where 0.98 wt-% is the alloy Mg composition. The initial equilibrium volume fraction of the β-phase was calculated by *Thermo-Calc* and is f_{β}^{0} = 1.63%.

The problem, described by Equations 1–9, was solved by the *DICTRA* methodology. In order to investigate the effect of the initial average size of the β-phase dispersion on dissolution kinetics, the simu-

lations were carried out for r_{β}^{0} = 2, 10, and 50 nm.

During the weld thermal cycle, the volume fraction of the β-Mg$_2$Si phase changes. The variation of f_{β} with time from t = 0 up to t = τ, where τ is the duration of the thermal cycle, for T_{max} = 595°C, is given in Figs. 6, 7, and 8 for initial sizes r_{β}^{0} = 2, 10, and 50 nm, respectively. In Fig. 6A, results for short cycles (up to 4 × 10⁻³ s) are depicted, while Fig. 6B depicts results for longer cycles (up to 0.15 s). In all cases the thermal cycle starts with dissolution during heating and ends
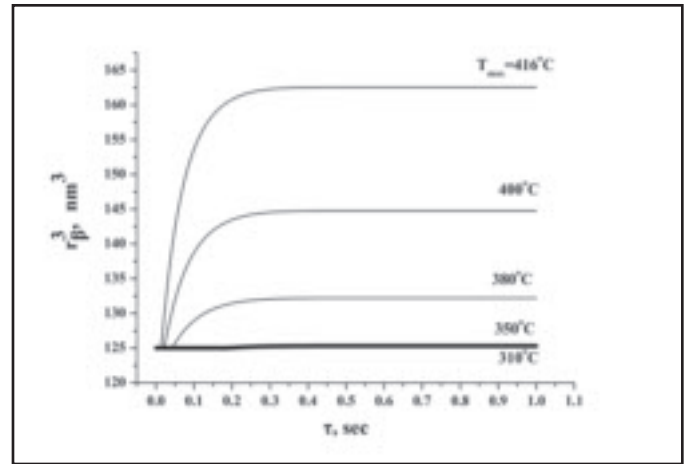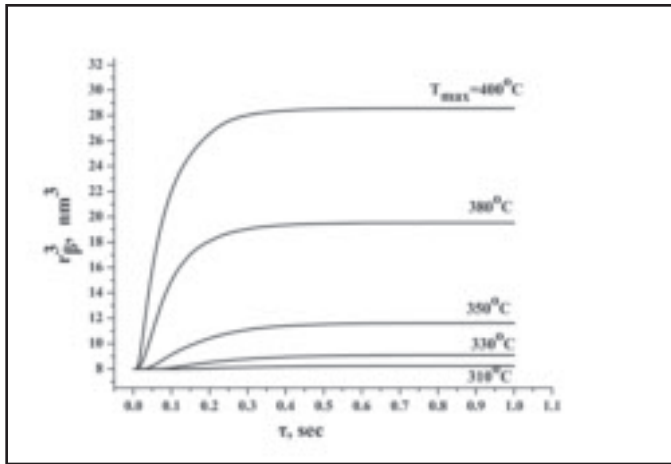
Fig. 14 — Variation of $\bar{r}_\beta^3$ vs. τ for various values of T_{max} ($r_\beta^0 = 2\ nm$).

Fig. 15 — Variation of $\bar{r}_\beta^3$ vs. τ for various values of T_{max} ($r_\beta^0 = 5\ nm$).

with reprecipitation during cooling. The dissolution rate is larger for short cycles. However, the extent of dissolution increases with the thermal cycle duration while full dissolution ($f = 0$) commences for cycles longer than 10^{-2} s. The amount of reprecipitation depends on the extent of dissolution, since dissolution increases supersaturation in Mg and Si and, therefore, increases the driving force for precipitation during the cooling part of the thermal cycle. The simulation results for the case where the initial dispersion of β has a mean size of 10-nm are shown in Fig. 7. Here complete dissolution commences for large cycle duration (Fig. 7B) where reprecipitation also appears. Reprecipitation for short cycles is low (Fig. 7A). This behavior can be attributed to the fact that the 10-nm dispersion is coarser than the 2-nm dispersion of β-phase and the respective diffusion distances are larger. The results for the 50-nm dispersion are shown in Fig. 8, where dissolution followed by reprecipitation is evident only for long cycles of the order of seconds.

The effect of initial dispersion size is shown clearly in Fig. 9 where the variation of the volume fraction of β-phase is compared for the three cases of initial mean size of dispersion for the same cycle duration $\tau = 7.8$ ms. The results show that the 50-nm dispersion is practically not affected by the thermal cycle, the 10-nm dispersion undergoes partial dissolution while during the same thermal cycle, and the 2-nm dispersion undergoes complete dissolution and a significant amount of reprecipitation.

While the above results show the variation of f_β during the thermal cycle, the final value of the volume fraction at the end of the thermal cycle (expressed as f_β / f_β^0) is shown as a function of thermal cycle duration τ in Fig. 10 for $T_{max} = 595°C$ for the three initial mean dispersion sizes of 2, 10, and 50 nm.

For a specific T_{max}, the general shape of these curves indicates that the final volume fraction of β-phase (at the end of the thermal cycle) first decreases for short cycles and then increases for longer cycles. The minimum in f_β / f_β^0 is shifted to longer cycles as the initial mean size of the dispersion increases from 2 to 50 nm. Regarding the effect of T_{max}, the minimum is shifted to lower values (greater extent of dissolution) with an increase in T_{max}.

The variation of the size r_β of the β-phase during the thermal cycle shows similar characteristics as the variation in volume fraction. Typical results are shown in Fig. 11, which depicts the final mean size of the dispersion as a function of thermal cycle duration τ, at $T_{max} = 595°C$ for the three initial dispersion mean size of 2, 10, and 50 nm. Again here, the final size first decreases and then increases with cycle duration. The minimum in r_β is shifted to longer cycles with increasing the initial dispersion mean size.

Simulation of Coarsening during Laser Welding of 6061-T6

The weld thermal cycle used in the coarsening simulations is depicted in Fig. 12. Due to *DICTRA* software requirements, the heating part of the thermal cycle was replaced by an equivalent isothermal part at T_{max} with duration τ_1 such that the areas below the *T, t* curves are the same — Fig. 12. The isothermal part is followed by a cooling part from T_{max} to T_i (room temperature) with a cooling rate H_c. The overall duration of the thermal cycle is τ. The values of the parameters of the thermal cycles used in the coarsening simulations, as calculated with the FEM method, are shown in Table 2.

Table 2 — Values of the Thermal Cycle Parameters Used for the Coarsening Simulations

T_{max} (°C)	H_C (°C/s)	τ_1 (s)	τ (s)
416	10^2-10^4	0.01	0.2–1
400	10^2-10^4	0.01	0.2–1
393	10^2-10^4	0.01	0.2–1
380	10^2-10^4	0.01	0.2–1
350	10^2-10^4	0.01	0.2–1

Table 3 — Comparison of Experimental and Calculated Microhardness Values for Certain Positions within HAZ_1

Position	f_β	r_β (nm)	Microhardness from calculations (HV)	Microhardness from measurements (HV)
A	0.0122	1.725	95.3	85
B	0.01173	1.70	92	83
C	0.01183	1.7029	92.8	85
D	0.01245	1.7424	96.6	85
E	0.013175	1.7975	100.6	87
F	0.014247	1.8692	106.6	88

For the simulations, the coarsening module in *DICTRA* was employed. According to this method coarsening of the dispersion can be described by considering one spherical particle, which has the maximum size of the dispersion prior to the application of the welding cycle. According to the LSW theory of coarsening (Refs. 20, 21), the maximum size r_p is 1.5 times the mean dispersion size $\bar{r}$. The geometrical model is shown in Fig. 13. The spherical particle of β-phase is embedded in a sphere of matrix α-phase. At the interface between α and β local thermodynamic equilibrium between α-phase and β-phase with radius r_p is assumed. In this case a Gibbs-Thomson contribution is added to the Gibbs free energy of the particle, which is

$$\frac{2\gamma V_m}{r_p} \quad (10)$$

where γ is the interfacial energy of the β particle in the α-phase and V_m the molar volume. At the spherical cell boundary the α-phase is in local equilibrium with β-phase particle of the mean size $\bar{r}$, so the contribution to the Gibbs energy in this case is

$$\frac{2\gamma V_m}{\bar{r}} \quad (11)$$

The difference in the Gibbs-Thomson contributions to the free energy causes diffusion of Mg and Si atoms toward the particle with radius r_p, which grows.

Due to the lower diffusivity of Mg in Al, coarsening was considered to be con-

trolled only by Mg diffusion. The interfacial energy γ was taken 0.5 Jm^{-2} (Ref. 11). In order to maintain constant volume fraction of β-phase and the initial overall alloy composition, the α-phase cell grows accordingly. For a given volume fraction f of the β-phase the relation between α and β radii is

$$r_\alpha = \left(\frac{1}{f_\beta^{1/3}} - 1\right) r_\beta \quad (12)$$

Characteristic results of the coarsening simulations are shown in Fig. 14 for the case where the initial mean dispersion size is 2 nm. The figure depicts the variation of cube mean size $\bar{r}^3$ as a function of cycle duration τ. The mean particle size increases with cycle duration, the change being more rapid for short cycles. For cycles longer than about 0.3 s, particle growth is very slow. As expected, coarsening kinetics is faster at higher T_{max}. Figure 15 depicts similar results for a dispersion of initial mean size 5 nm. Compared to the previous case of 2 nm, coarsening kinetics is slower because the initial dispersion is coarser.

Comparison with Experimental Hardness Profiles in the HAZ

In this section a comparison is attempted between calculated hardness profiles and experimental ones. The calculation of hardness is based on the hard-

ness of the base metal reduced by an amount depending on the extent of dissolution or coarsening in the HAZ. These in turn depend on the final values of f_β and r_β in the HAZ.

Hardness Profiles in HAZ_1

Figure 16 depicts all the elements necessary for the comparison of the calculated and experimental hardness profiles in HAZ_1. The experimental hardness profile was measured after laser welding with the following conditions: laser power 4.5 kW, laser travel speed 4.8 m/min, and focal distance –1 mm. In Fig. 16 the variation of the following is shown:

• Hardness profiles (i.e., hardness at points A, B, C, D, E, and F of HAZ_1), in Fig. 16A.

• The maximum temperature T_{max} and the duration of the thermal cycle τ for each respective point in HAZ_1, in Fig. 16B.

• The volume fraction f_β of phase β-Mg_2Si at each point at the end of thermal cycle, in Fig. 16C.

• The size r_β of phase β-Mg_2Si at each point at the end of thermal cycle, in Fig. 16D.

The hardness of the base metal is $H_B =$ 118 HV, while for the 6061-T6 used in this study, the precipitate has $f_\beta^0 =$ 1.63% and $r_\beta^0 =$ 2nm. The experimental hardness profile shows that welding is accompanied by

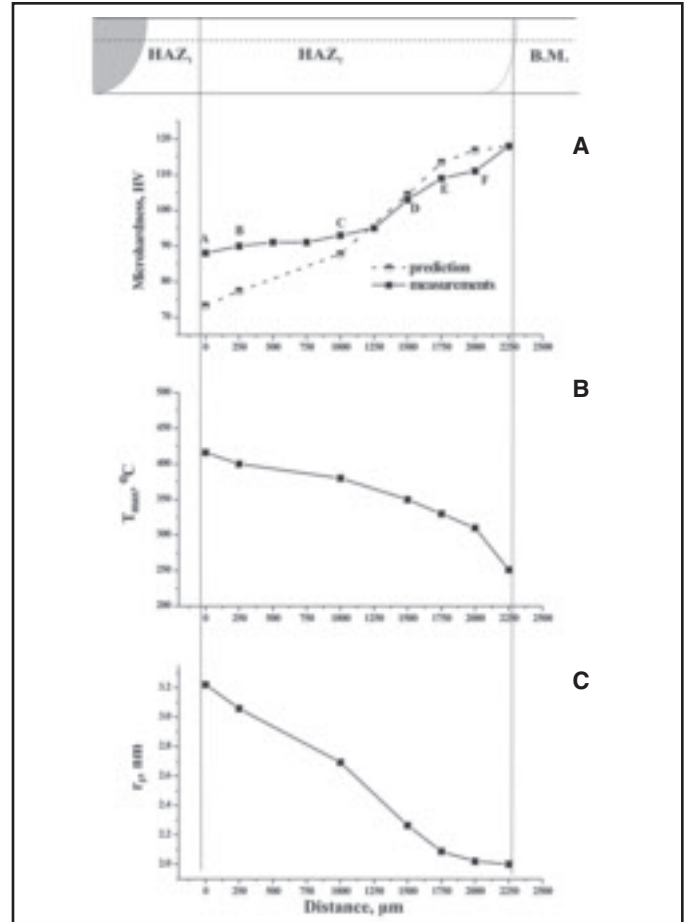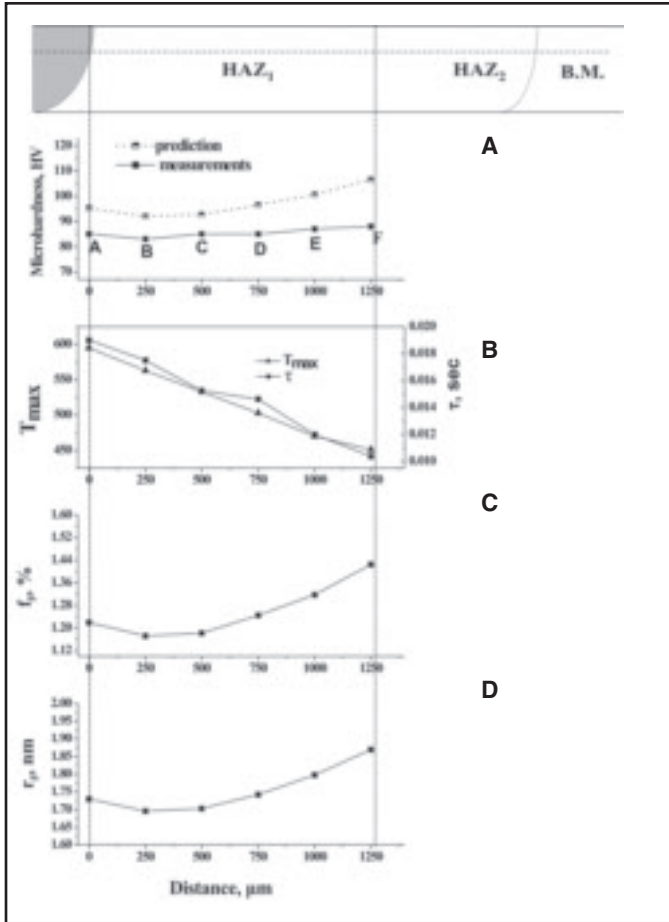Fig. 16 — A — Experimental and predicted microhardness profile in the HAZ$_1$; B — T$_{max}$ and thermal cycle duration; C — volume fraction; D — size of β phase calculations at certain positions within HAZ$_1$.

Fig. 17 — A — Experimental and predicted microhardness profile in the HAZ$_2$; B — T$_{max}$; C — size of β phase calculations at certain positions within HAZ$_2$.

a reduction of hardness in HAZ$_1$. More specifically, the hardness is 88 HV at the boundary with HAZ$_2$ (point F), drops to 83 HV in point B, and increases to 85 HV at the fusion zone boundary (point A). The maximum temperature of the thermal cycle T_{max} increases from 451°C at point F to 595°C at point A. The respective heating and cooling rates for these points are H_R = 12000°C/s, H_C = 8326°C/s for point F, and H_R = 24375°C/s, and H_C=17727°C/s for point A, while the respective cycle lengths are $τ_F$ = 0.01038 s and $τ_A$ = 0.019 s. The values of T_{max}, H_R, H_C, and τ are the input parameters of the thermal cycle for the simulation of dissolution. The simulation provides the values of $f_β$ and $r_β$ at the end of the thermal cycle

for points A to F. The results are plotted in Fig. 16C and D, respectively. Precipitation hardening in HAZ$_1$ comes from two contributions:

• Coherency hardening, which is proportional to f ^{½}r ^{½}, and

• Orowan hardening (obstacle bypassing), which is proportional to f ^{½}r^{-1}.

The change in hardness (ΔH) due to dissolution of β-phase relative to the hardness of the base metal (H_{BM}) is given by

$$\frac{\Delta H}{H_{BM}} = \frac{\left(f_β r_β\right)^{1/2} - \left(f_β^0 r_β^0\right)^{1/2}}{\left(f_β^0 r_β^0\right)^{1/2}}$$

$$+ \frac{f_β^{1/2} r_β^{-1} - \left(f_β^0\right)^{1/2}\left(r_β^0\right)^{-1}}{\left(f_β^0\right)^{1/2}\left(r_β^0\right)^{-1}}$$

(13)

where $f_β^0$ =1.63% and $r_β^0$ = 2 nm for the condition T6.

The hardness for each point of HAZ$_1$ is calculated by the expression

$$H = H_{BM} + \left(\frac{\Delta H}{H_{BM}}\right)H_{BM}$$

(14)

The results for each point of HAZ$_1$ are shown in Table 3. The calculated hardness values are plotted with the experimental values in Fig. 16A. The simulation underestimates the softening of the HAZ by 8–10%. This is attributed to the fact that only dissolution was accounted for the observed softening. Taking into account all the assumptions made for the current simulation, the comparison with the experimental results is satisfactory.

Table 4 — Comparison of Experimental and Calculated Microhardness Values for Certain Positions within HAZ$_2$

Position	T_{max}	r_β (nm)	Microhardness from calculations (HV)	Microhardness from measurements (HV)
A	416	3.22	73.3	88
B	400	3.05	77.3	90
C	380	2.69	87.7	93
D	350	2.26	104.4	103
E	330	2.08	113.4	109
F	310	2.02	116.8	111

Hardness Profiles in HAZ$_2$

In HAZ$_2$ the maximum temperature T_{max} does not exceed 400°C and only coarsening was considered to take place. As stated in the introduction, although the primary strengthening phases are the metastable phases β″ and β′, only the equilibrium precipitate β-Mg$_2$Si was considered in the simulations, since kinetic data for the metastable phases (β″, β′) are not yet included in the relevant databases.

Taking the above into consideration, hardness changes are attributed to the coarsening of the β phase. Figure 17 shows the variation of the following:

• Hardness profiles (i.e., hardness at points A, B, C, D, E, and F of HAZ$_2$), in Fig. 17A.

• The maximum temperature T_{max} for each respective point in HAZ$_2$, in Fig. 17B.

• The size r_β of phase β-Mg$_2$Si at each point at the end of the thermal cycle, in Fig. 17C.

The experimental hardness profile in Fig. 17A shows that the hardness drops from 118 HV in the base metal to 88 HV at the boundary with HAZ$_1$ (point A). The coarsening simulation shows that the size of the β-Mg$_2$Si phase increases from 2 nm in the base metal to 3.22 nm at point A. In order to calculate the hardness at each point in HAZ$_2$, it is considered that only the Orowan mechanism is active (overaging conditions). For this case, hardening is proportional to $f^{1/2}r^{-1}$. During coarsening the volume fraction f remains constant for all points of HAZ$_2$. Therefore, the hardness of points A to F in HAZ$_2$ is calculated by

$$H = \frac{H_{BM}\, r_\beta^0}{r_\beta}$$

(15)

The calculated values are given in Table 4 and are shown in Fig. 17A. Again, taking into account the assumptions made, the comparison between the calculated and experimental values is satisfactory.

Conclusions

The softening of the HAZ following laser welding of 6061-T6 Al-alloy has been successfully predicted by the simulation of dissolution, reprecipitation, and coarsening of the strengthening precipitates during the weld thermal cycle. A finite element based analysis of heat flow was employed for the calculation of thermal cycles.

The computational kinetics software *DICTRA* was employed for the calculation of the variation of volume fraction and mean size of the precipitates during the welding thermal cycle under nonisothermal conditions.

Taking into account the limitations

stated in the paper, the calculated hardness profiles in the HAZ are in good agreement with the experimental values.

References

1. Tempus, G. 2001. Werkstoffe fur transport und verkehr, Materials Day, ETH, Zurich, Switzerland.

2. Zink, W. 2004. Opening lecture at the Mesomechanics Conf. 2004, University of Patras, Greece.

3. Zervaki, A. D. 2004. Laser welding of aluminum alloys: experimental study and simulation of microstructure evolution in the HAZ, PhD dissertation. University of Thessaly, Greece.

4. Kou, S. 2003. *Welding Metallurgy*. pp. 359–362, Hoboken, N.J., John Willey & Sons Inc.

5. Malin, V. 1995. Aluminum welded joints, study of metallurgical phenomena in the HAZ of 6061-T6. *Welding Journal* 74(9): 305-s to 318-s.

6. Engstrom, A., Hoglud, I., and Agren, J. 1994. Computer simulation of diffusion in multiphase systems. *Metallurgical Materials Transactions*. Vol. 25 A, pp. 1127–1134.

7. Vermolen, F. J., and Vuik, C. 2000. A mathematical model for the dissolution of particles in multi-component alloys. *Journal of Computational and Applied Mathematics*. Vol. 26, pp. 233–254.

8. Bratland, D. H., Grong, O., Schercliff, H., Myhr, O. R., and Tjotta, S. 1997. Modelling of precipitation reactions in industrial processing. *Acta Materialia*. Vol. 45, pp. 1–22.

9. Nicolas, M., and Deschamps, A. 2003. Characterization and modelling of precipitate evolution in an Al-Zn-Mg alloy during nonisothermal heat treatments. *Acta Materialia*. Vol. 51, pp. 6077–6094.

10. Grong, O., and Myhr, H. 2000. Modelling of nonisothermal transformations in alloys containing a particle distribution. *Acta Materialia*. Vol. 45, pp. 1– 22.

11. Grong, O. 1997. *Metallurgical Modelling of Welding*. pp. 325–334, The Institute of Materials, Cambridge University Press, UK.

12. Ion, J. C., Easterling, K. E., and Ashby,

M. F. 1984. A second report on diagrams of microstructure and hardness for HAZ in welds. *Acta Materialia*. Vol. 32, pp. 1949–1962.

13. Bjorneklett, B. I., Grong, O., Myhr, H., and Kluken, A. O. 1998. Additivity and isokinetic behavior in relation to particle dissolution. *Acta Materialia*. Vol. 46, pp. 6257–6266.

14. Nicolas, M., and Deschamps, A. 2002. Precipitate microstructure in the heat-affected zone of Al-Mn-Mg MIG-welds and evolution during post welding heat treatments. *Materials Science Forum*. Vol. 396–402, pp. 1561–1566.

15. Agren, J. 1990. Kinetics of Carbide dissolution. *Scandinavian Journal of Metallurgy*. Vol. 9, pp. 2–8.

16. Gustafson, A. 2000. Aspects of microstructural evolution in chromium steels in high temperature applications. PhD dissertation. KTH Sweden.

17. Gustafson, A., Hoglud, L., and Agren, J. 1998. Simulation of carbo-nitride coarsening in multicomponent Cr-steels for high temperature applications. *Advanced Heat Resistant Steels for Power Generation*. IOM Communications Ltd., London, pp. 270–276.

18. Gustafson, A. 2000. Coarsening of TiC in austenitic stainless steel — experiments and simulations in comparison. *Materials Sci. Eng.* Vol. A287, pp. 52–58.

19. Prikhodovski, A., Hurdado, I., Spencer, P. J., and Neuschutz, D. 1998. Mathematical simulation of microstructure coarsening during preheating of aluminium alloys. *Proc. 5th Intl Conference on Semi-Solid Processing of Alloys and Composites*, Colorado, pp. 249–256.

20. Lifshitz, I. M., and Slyozov, V. V. 1961. The kinetics of precipitation from supersaturated solid solutions, *J. Phys. Chem. Solids*. 19, pp. 35–50.

21. Wagner, C. 1961. Theorie der Altrung von Nieederschlagen durch Umblosen (Ostwald-Reinfund), *Z. Electrochem*. 65, pp. 581–591.

22. *ABAQUS*. 1997. Hibbit, Karlsson & Sorensen, Inc., Pawtucket, R.I.

23. Sudman, B., Jonsson, B., and Andersson, J.-O. 1985. The thermo-calc databank system. *CALPHAD*. Vol. 9, p. 153.

CAN WE TALK?

The *Welding Journal* staff encourages an exchange of ideas with you, our readers. If you'd like to ask a question, share an idea or voice an opinion, you can call, write, e-mail or fax. Staff e-mail addresses are listed below, along with a guide to help you interact with the right person.